Available online at www.sciencedirect.com

ScienceDirect

Trans. Nonferrous Met. Soc. China 35(2025) 2304−2319

Transactions of
Nonferrous Metals
Society of China

www.tnmsc.cn

Mechanical properties and microstructural evolution of nickel-based superalloys

Wu-qiang HE[1,2,3], Ping KE[1], Jing-yue HUANG[1], Feng LIU[2,3],
Li-ming TAN[2,3], Lan HUANG[2,3], Shi-wen HE[1], Cui LAI[4], Cai-he FAN[1]

1. College of Materials and Advanced Manufacturing, Hunan University of Technology, Zhuzhou 412007, China;
2. State Key Laboratory of Powder Metallurgy, Central South University, Changsha 410083, China;
3. Powder Metallurgy Research Institute, Central South University, Changsha 410083, China;
4. College of Environmental Science and Engineering, Hunan University, Changsha 410083, China

Received 1 December 2023; accepted 27 September 2024

Abstract: The mechanical properties and oxidation resistance of two nickel-based superalloys with and without oxide dispersion strengthened (ODS) phases at different temperatures were studied. The microstructure was investigated by scanning electron microscopy (SEM), electron backscatter diffraction (EBSD), and transmission electron microscopy (TEM). The results show that the yield strength of the samples with and without ODS phases at room temperature is 1020 and 324 MPa, respectively. The yield strength model was constructed, and it is found that the contribution of grain boundary strengthening, dislocation strengthening and nanoparticle strengthening of nickel-based ODS superalloy exceeds 83%. As the temperature increases, grain boundary sliding and migration decrease the strength of sample but improve its ductility. Oxidation hinders the ductility of sample and intensifies its fracture, and the maximum elongation of nickel-based ODS superalloy at 800 °C is 47.3% .

Key words: nickel-based superalloys; oxide dispersion strengthened (ODS) phase; mechanical properties; oxidation resistance

1 Introduction

Nickel-based superalloys have been considered as promising candidate materials to fulfill the corrosion, oxidation and creep challenges imposed by the operating environment of components such as gas turbines and heat exchanger tubing [1−3]. It is well known that the dispersed nanoparticles and grain size of nickel-based superalloys are crucial factors in improving their properties [4,5]. Nickel-based oxide dispersion strengthened (ODS) superalloys are conventionally produced by mechanical alloying (MA) and hot extrusion (HEX) [6]. In order to form nanoparticles in the matrix, pure elemental powder or pre-alloyed powder is usually combined with a small number of thermally stable oxide particles (such as La_2O_3, Ce_2O_3, ZrO_2 and Y_2O_3) by ball milling, which can refine grains and precipitate nanoparticles, such as La−Al/Ti−O, Ce−Al/Ti−O, Y−Al/Ti−O, and Y−Zr−O [7−9]. The dispersed oxide particles can also hinder movement of grain boundary (GB) and dislocations, thereby improving the strength of the alloy [10,11].

The frequent cracking of nickel-based superalloys in elevated-temperature environments is the main factor limiting the use of these superalloys [12,13]. Therefore, the ductility of nickel-based superalloys, which is easily decreased in elevated-

---

Corresponding author: Cai-he FAN, Tel: +86-13787062698, E-mail: 369581813@qq.com;
Feng LIU, Tel: +86-13637494795, E-mail: liufeng@csu.edu.cn

https://doi.org/10.1016/S1003-6326(25)66816-6

temperature oxygen environments, requires special consideration. GB is a source of weakness at elevated-temperatures due to its interaction with gaseous environments containing oxygen and can easily slide and migrate leading to instability, and the pinning effect of nanoparticles on GB and dislocations weakens with increasing temperature [14]. Generally, the ductility of the nickel-based superalloys without ODS decreases with increasing temperature, reaching its lowest value around 800 °C, and then gradually recovering. Two primary mechanisms, namely dynamic embrittlement (DE) and stress accelerated grain boundary oxidation (SAGBO), frequently explain the cause of the ductility loss in nickel-based superalloys at elevated temperatures [15−18]. All the conditions for cracking in both mechanisms are considered, including oxygen, applied load, and high temperature. Interestingly, the peak ductility of ultra-fine grain (UFG) nickel-based ODS superalloys is observed at about 800 °C, indicating that the mechanism of influence of ductility in nickel-based ODS superalloys differs from that of nickel-based superalloys without ODS. Meanwhile, the influence mechanism of ductility and oxidation resistance of nickel-based ODS superalloys has rarely been reported, and the evolution of microstructure, mechanical properties and oxidation resistance of nickel-based ODS superalloys at different temperatures is still unclear, which urgently requires in-depth research.

In this study, a systematic examination of their tensile properties and oxidation resistance at different temperatures was carried out. The contributions of grain boundary strengthening, dislocation strengthening and nanoparticle strengthening of the nickel-based superalloy were calculated, and the room temperature (RT) yield strength model was constructed. This work aims to reveal the influence mechanism of strengthening and toughening of nickel-based superalloys with and without ODS.

2 Experimental

2.1 Materials

Two kinds of nickel-based pre-alloyed powders, PA1 and PA2, prepared by argon atomization were used in this study. Table 1 lists the chemical compositions of the pre-alloyed powder. The MA powder was prepared by ball milling PA1 and 0.6 wt.% YH_2 powder for 24 h at a speed of 350 r/min under the protection of high purity argon gas (99.999%). The mass ratio of ball to powder was 8:1, and 0.5 wt.% alcohol was added as process control agent to minimize powder agglomeration and cold-welding during ball milling. The PA2 and MA powders were canned in stainless steel containers and degassed at 400 °C for 12 h under a vacuum of 0.133 Pa, respectively. The containers were hot extruded at 1130 °C with an extrusion ratio of 16:1 followed by air cooling, named PA-NODS and MA-ODS, respectively.

Table 1 Chemical composition of pre-alloyed powder (wt.%)

Powder	Al	Cr	Fe	Ti	Y	C	Ni
PA1	0.25	20.5	0.67	0.56	0	0.054	Bal.
PA2	0.25	21	0.85	0.57	0.68	0.059	Bal.

2.2 Assessment of tensile property and fractography

Tensile tests were performed at temperatures ranging from RT to 1000 °C using an electronic universal testing machine (UTM5105, China) at a strain rate of $1\times10^{-3}\ s^{-1}$. A minimum of three tests were performed under each condition. The specimens (3.3 mm (width) × 26 mm (length) × 3 mm (thickness)) were prepared by wire-based electrical discharge machining along the longitudinal direction. Fracture morphologies were characterized using a scanning electron microscope (SEM, Quanta 650, FEI, USA) equipped with electron backscatter diffraction (EBSD) and energy dispersive spectrometer (EDS).

2.3 Measurement of oxidation damage

The samples with dimensions of 5 mm × 5 mm × 10 mm were exposed to a temperature ranging from 600 to 1000 °C with an interval of 100 °C for 1 h. Prior to isothermal exposure, the surfaces of the samples were ground to a 2000 grit finish using silicon carbide abrasive paper. SEM was used to observe the surface images of the samples. The 3D surface morphologies after oxidation were constructed from the depth information obtained from the contrast in the SEM images. The original 800×1000 pixel images were compressed to 20×25 matrix by taking one point in every 40 pixels. To avoid noise in the calculated results, the contrast value of each point is the average of 20×20 pixels around it. The calculated surface depth was normalized from 0 to 1, representing the lowest to the highest surface. The construction of 3D surface morphologies was performed using the Python open source code package [19].

2.4 Microstructure analysis

EBSD was used to detect the microstructure of the samples at accelerating voltage of 20 kV, with step size of 0.05 μm or 1 μm. The EBSD specimens were mechanically polished to 2000 grit finish using silicon carbide abrasive papers and 0.3 μm aluminium oxide, followed by vibratory polishing for 2−5 h by using a Buehler vibratory polisher VibroMet 2 (Buehler, USA) with 30% amplitude. The data were analyzed via HKL Channel 5 software and the equivalent grain size was determined based on the grain area (A), $2\sqrt{A/\pi}$.

The crystal structures and chemical compositions of nanoparticles were characterized by transmission electron microscopy (TEM, Themis Z 3.2, FEI, USA) and energy dispersive X-ray spectroscopy with an accelerated voltage of 300 kV. The TEM samples were polished to a thickness of 50 μm, and cut to diameter of 3 mm. Then, these discs were twin-jet electropolished at −25 °C and 40 V in the corrosive solution of 90% ethanol and 10% perchloric acid.

3 Results

3.1 Microstructure

The grain size and distribution of PA-NODS were characterized by EBSD inverse pole figure (IPF) maps, as illustrated in Figs. 1(a, b). PA-NODS has an equiaxed crystal structure, with a grain size of 1−40 μm and an average size of 10.2 μm. Meanwhile, the UFG and a few micron grains are detected in MA-ODS, with a size range from several hundred nanometers to 2.5 μm with an average grain size of 0.56 μm, as shown in Figs. 1(c, d).

Moreover, the TEM images are further used to analyze the microstructure of the samples. High-density dislocations are observed in PA-NODS, as shown in Fig. 2(a). The detailed information on the microstructure of MA-ODS is given in Figs. 2(b, c).

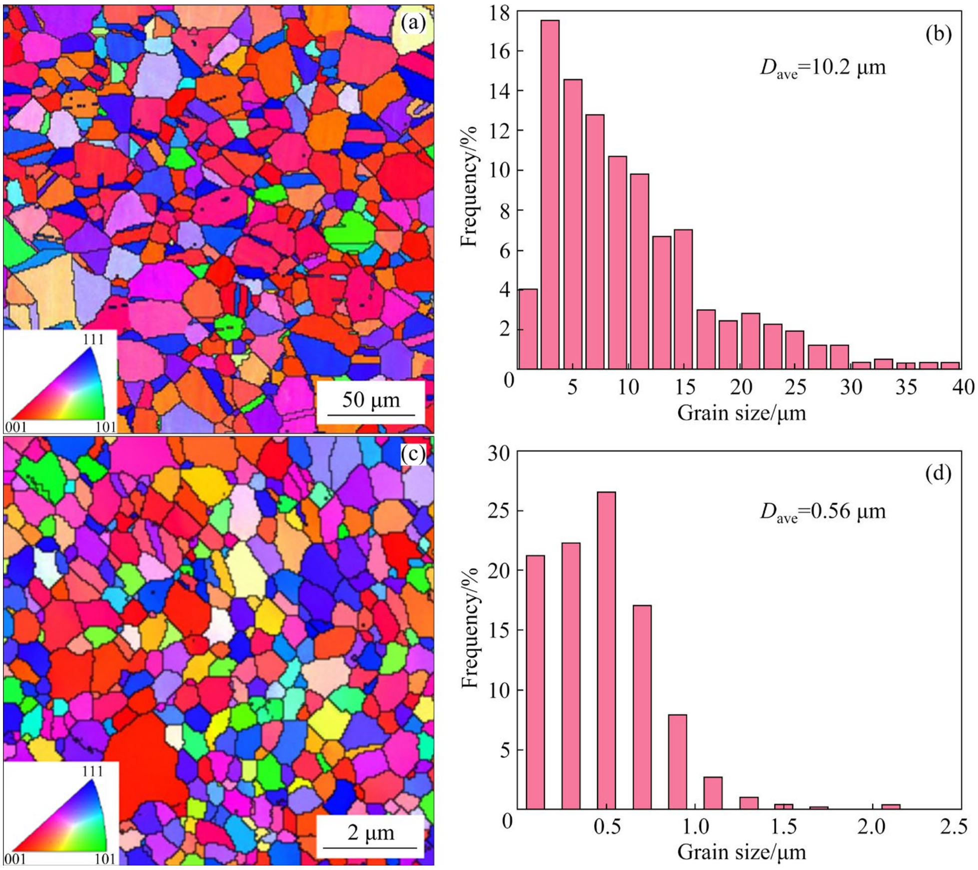

Fig. 1 IPF maps (a, c) and grain distribution (b, d) of samples: (a, b) PA-NODS; (c, d) MA-ODS

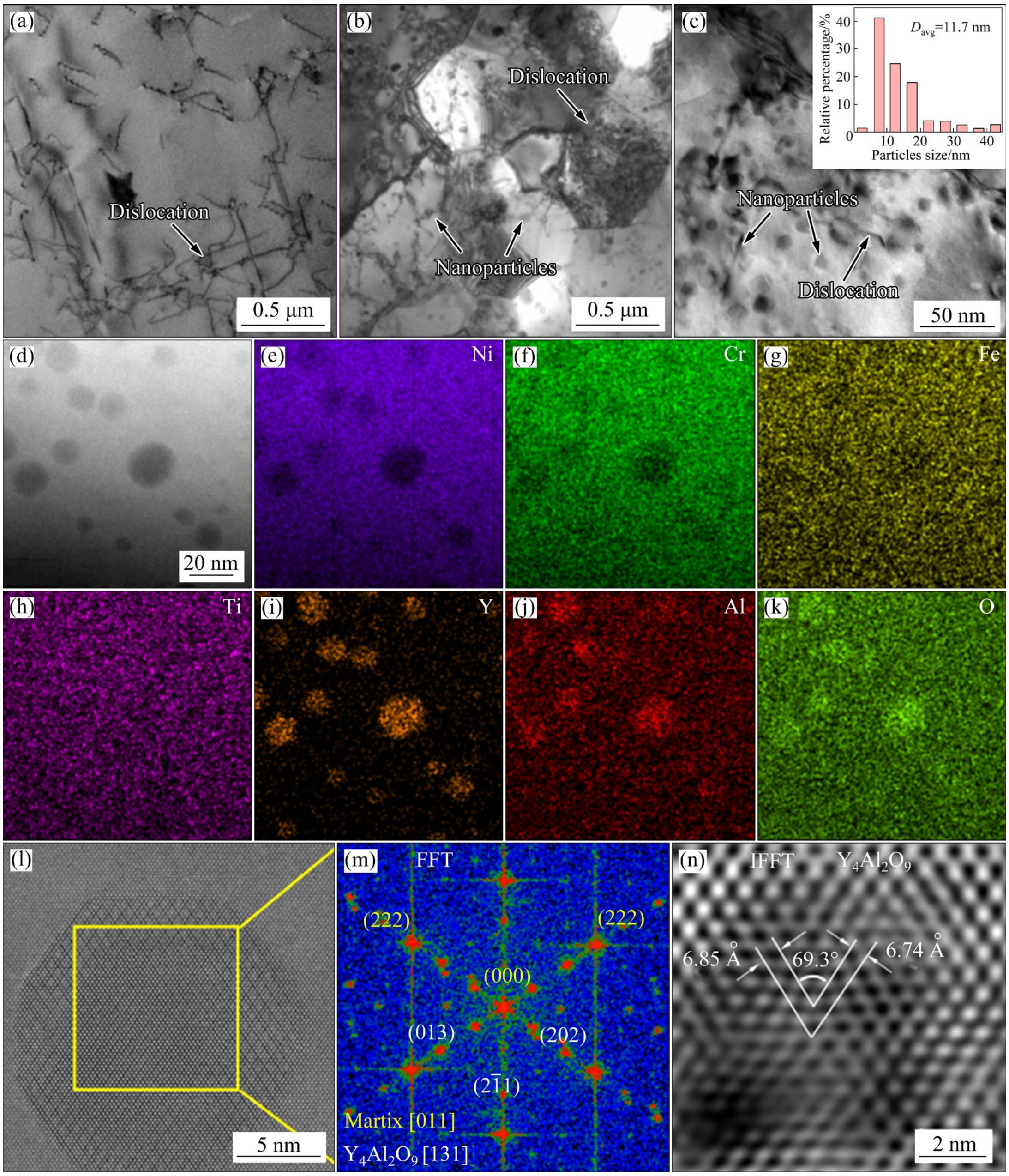

Fig. 2 Microstructures of PA-NODS (a) and MA-ODS (b−n): (a, b) TEM images; (c) TEM images and nanoparticle size distribution; (e−k) HAADF image and corresponding EDS results; (l−n) HRTEM image, FFT and IFFT patterns of nanoparticle, respectively

The alloy contains high-density dislocations and dispersed nanoparticles, some of which have spherical or faceted shapes and interact with the dislocations. Figure 2(c) (top right corner) exhibits the statistical histograms of the nanoparticle size distribution obtained by analyzing more than 500 nanoparticles from TEM micrographs. The nanoparticle size ranges from 2 to 50 nm with an average size of 11.7 nm. The high-angle annular dark field (HAADF) image and corresponding EDS elemental maps of nanoparticles in MA-ODS are presented in Figs. 2(d−k), and the corresponding elemental maps show that Y, Al and O are rich in these nanoparticles, and the segregation of other elements is not obvious. A high-resolution transmission electron microscope (HRTEM) is used to further determine the crystal structure of the nanoparticles, and a nanoparticle of about 20 nm is probed, as shown in Fig. 2(l). The diffraction pattern of nanoparticle is revealed by the corresponding Fast Fourier Transform (FFT) and Inverse Fast Fourier Transform (IFFT), as shown in

Figs. 2(m) and 2(n), respectively. The nanoparticle is identified as $Y_4Al_2O_9$ (YAM) with a zone axis of $[\bar{1}3\bar{1}]$.

3.2 Tensile property

Tensile tests were carried out from RT to 1000 °C in air. The ultimate tensile strength (UTS) and yield strength (YS) of the specimens are shown in Fig. 3(a). The curves can be divided into three regimes, namely low-temperature regime (≤600 °C), medium-temperature regime (600−800 °C) and elevated-temperature regime (≥800 °C). Notably, the strength of MA-ODS is higher than that of PA-NODS at test temperatures. YS values of MA-ODS and PA-NODS at RT are 1020 and 324 MPa, respectively. As expected, the strength of MA-ODS is superior to PA-NODS at low-temperature regime, due to the contribution of UFG, nanoparticles and dislocations in MA-ODS. YS values of MA-ODS and PA-NODS at 800 °C are 206.1 and 158.9 MPa, respectively. The strength gap between the two alloys decreases gradually due to the failure of grain boundary strengthening at temperature above $0.3T_m$, although dispersion strengthening is still effective at $0.9T_m$ [20]. Meanwhile, UFG is detrimental to the deformation resistance due to grain boundary (GB) sliding at elevated-temperature. Furthermore, coarse grain (CG) exhibits superior ability to store dislocations and work-hardening capacity, thereby mitigating the strength degradation of PA-NODS.

Figure 3(b) presents the elongation evolution of the specimens. Similar to the division of temperature interval, three regimes are noted. Here, the trends in ductility evolution differ significantly between the two alloys. As expected, except at 800 °C, the elongation of PA-NODS is significantly higher than that of MA-ODS, which is attributed to the CG microstructure of PA-NODS. Usually, the ductility−brittleness transition temperature (DBTT) can be assessed by the effective grain size [21]. Large grains have long crack propagation paths, leading to a high ductility of the material [22]. The ductility of PA-NODS initially decreases and then increases with increasing temperature, reaching a minimum value of 38%, and recovering with

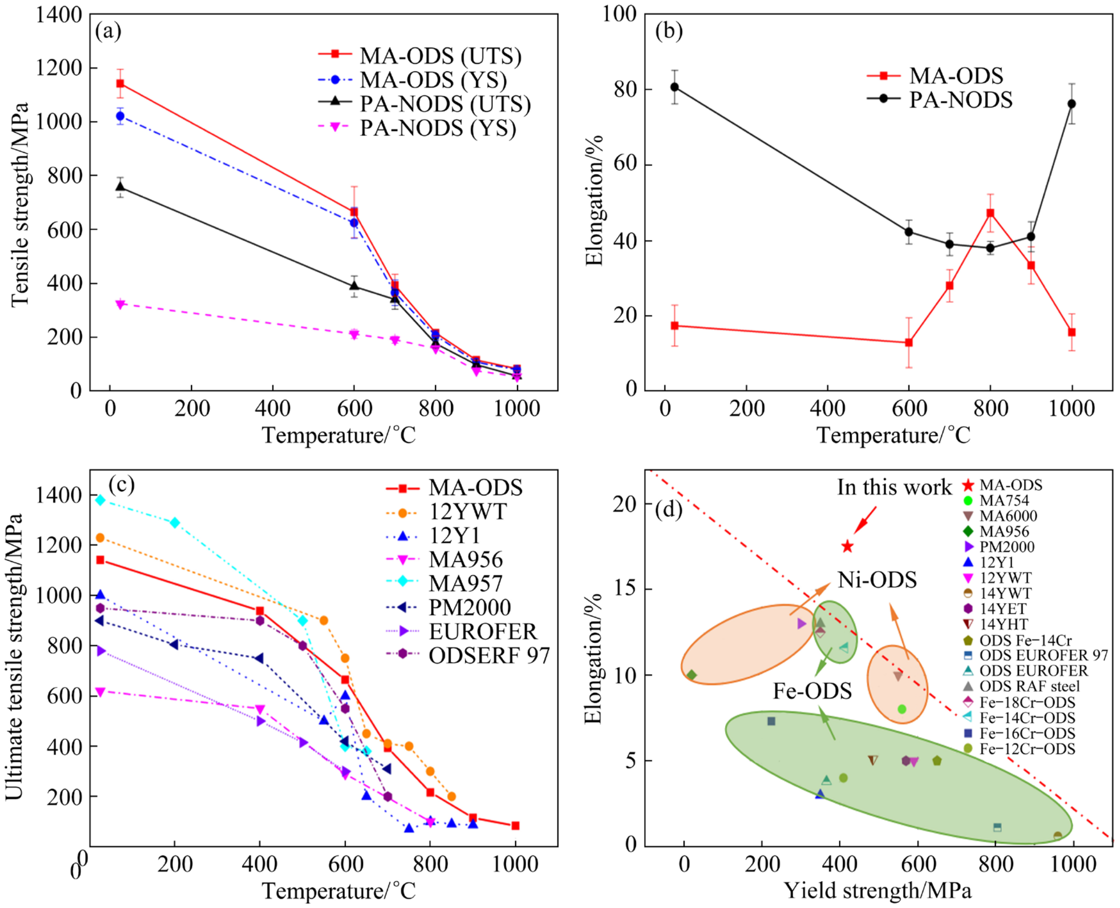

Fig. 3 Tensile strength (a) and elongation (b) of samples at different temperatures; comparison results of UTS at different temperatures (c) and yield strength and elongation at RT (d) between MA-ODS and other ODS superalloys

increasing temperature. For MA-ODS, there is no significant variation in the elongation in the low-temperature regime of MA-ODS, whereas the elongation of PA-NODS decreases significantly. In the medium-temperature regime, the elongation of MA-ODS increases significantly, reaching a maximum value of 47.3%. In the elevated-temperature regime, the elongation of MA-ODS decreases, whereas the elongation of PA-NODS improves significantly above 900 °C. The results suggest that the mechanisms of influencing the ductility of MA-ODS and PA-NODS are different, the mechanisms behind which will be discussed thereafter.

Figures 3(c, d) show comparisons of MA-ODS and other ODS superalloys in the literature [23−33]. As shown in Fig. 3(c), when the temperature is below 600 °C, the strength of MA-ODS is only inferior to that of MA957 and 12YWT and far superior to that of ODS superalloys, such as PM2000 and MA956. As the temperature is above 600 °C, the strength of MA-ODS is only inferior to that of 12YWT. In addition, considering the YS and elongation of alloys at RT, as shown in Fig. 3(d), the alloy in the upper right corner has superior mechanical properties. Although 12YWT has the highest strength, its elongation is only ~5%. The YS and elongation of PM2000 at RT are only ~900 MPa and 12%, respectively. Other ODS superalloys such as MA956 and 14YWT have higher strength but lower elongation. MA-ODS has a slightly lower yield strength than 12YWT, but its elongation is much higher than that of 12YWT. Generally, MA-ODS has good comprehensive mechanical properties compared to other ODS superalloys such as 14YWT and EUROFER which have only high strength or plasticity.

3.3 Relationship between microstructure and mechanical property

Figure 4 shows the fracture surfaces of the specimens that ruptured at different temperatures.

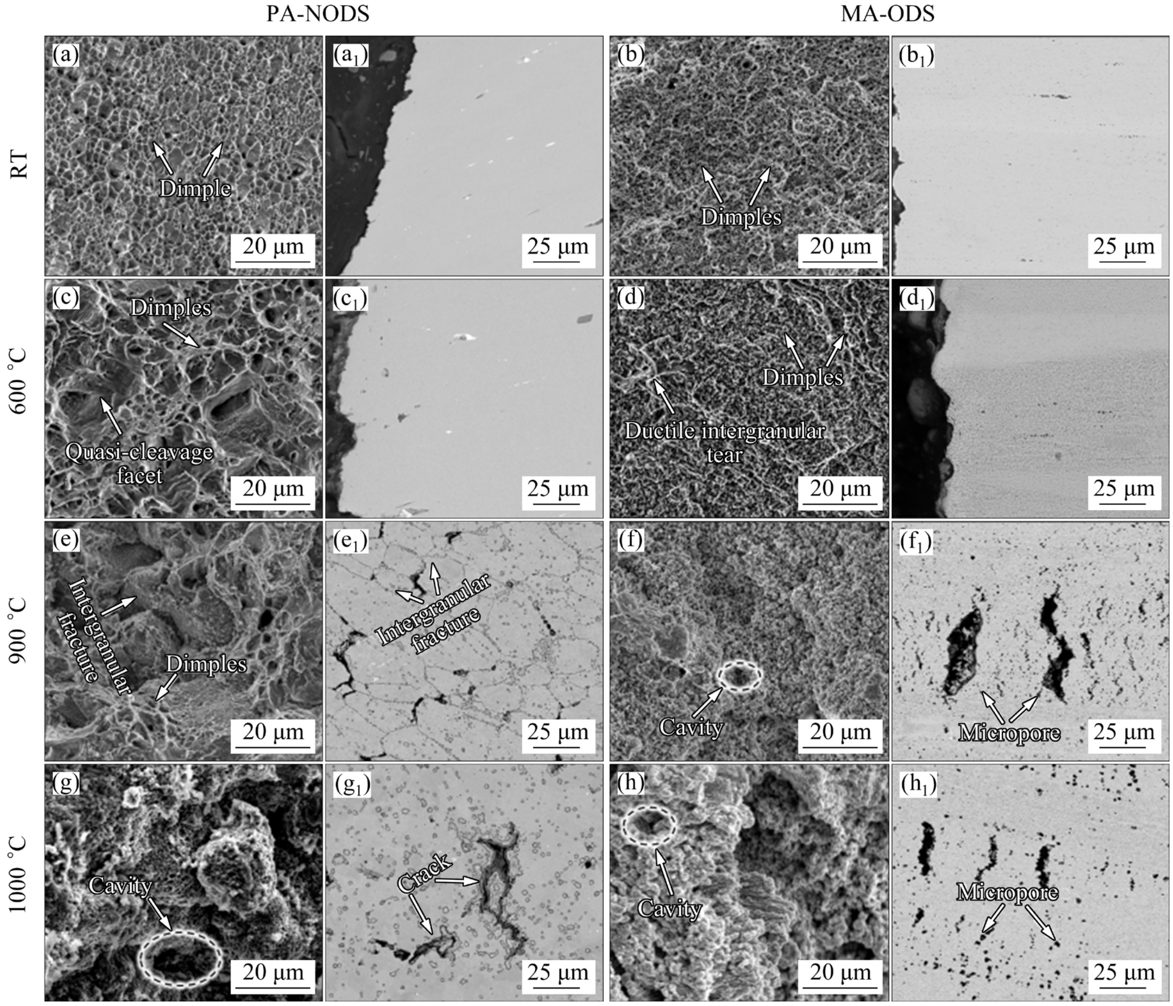

Fig. 4 SEM images of fracture surfaces (a−h) and cross-sections (a_1−h_1) of PA-NODS (a, a_1, c, c_1, e, e_1, g, g_1) and MA-ODS (b, b_1, d, d_1, f, f_1, h, h_1) ranging from RT to 1000 °C

Many dimples are observed in the specimens tested at RT, as shown in Figs. 4(a, b), and the size of these dimples is consistent with the grain size, indicating a significant transgranular fracture characteristic. The micrometer dimples of PA-NODS exhibit outstanding ductility, while the nanoscale dimples of MA-ODS also reflect its inferior ductility compared to PA-NODS.

At 600 °C, as shown in Figs. 4(c, d), the dimples are still the main morphological features of the fracture surfaces in PA-NODS, although the quasi-cleavage facets are also visible, indicating a shift in the deformation mechanism of PA-NODS. Similar to the fracture morphology of MA-ODS at RT, nano-sized dimples and a few ductile intergranular tears are detected.

As the temperature increases to 800 °C, mixed characteristics of dimples, intergranular fracture and cavities are observed in PA-NODS, as described in Fig. 4(e). The cross-sections of the failure specimens are further used to analyze the fracture mechanism, as shown in Fig. 4(e_1). Intergranular fracture is observed in PA-NODS, and there is a transition between ductile transgranular and quasi-brittle intergranular failure. The intergranular crack propagation limits the ductility, which explains the loss of ductility of PA-NODS in the medium-temperature regime. Figures 4(f, f_1) show the fracture surfaces of MA-ODS. The cavities are formed and expand into cracks under the loading stress, resulting in material failure. These observed cavities indicate that plastic deformation has occurred primarily by cavity nucleation and growth rather than homogeneous plastic flow.

Compared to the fracture morphology at 800 °C, the intergranular fracture disappears, and significant cavities are observed in PA-NODS at 1000 °C, as shown in Figs. 4(g, g_1), indicating that the deformation mechanism has changed again. Figures 4(h, h_1) show the fracture morphology of MA-ODS, and no significant change is detected except for the obvious oxidation at elevated temperature.

Moreover, to further investigate the internal microstructure distortion and damage during the tensile test, EBSD was used to estimate the geometrically necessary dislocations (GNDs) distribution at specific damage sites at 800 and 1000 °C, as shown in Fig. 5. The density of GNDs can be calculated by the following expression [34]:

$$\rho_{\mathrm{d}}=2\theta/(\mu b) \tag{1}$$

where μ is the unit length, b is the magnitude of Burgers vector and θ is the misorientation angle estimated on the basis of the kernel average misorientation (KAM) map [34].

At 800 °C, distinct high KAM values are observed at GBs of PA-NODS, especially at the triple junctions with poor plastic incompatibility, as indicated by the red circles in Fig. 5(a_2). This indicates high dislocation density there, which is consistent with the other nickel-based superalloys [35−37]. Some cracks are formed at the triple junctions with significant stress concentration. With the temperature increasing to 1000 °C, the KAM value decreases significantly, and the high KAM value is concentrated in the grains, as shown in Figs. 5(b_1, b_2). Moreover, the characteristic of elongated GBs aligning at 45° to the tensile loading axis indicates the occurrence of GB sliding and migration. Compared to the PA-NODS, the KAM value of the MA-ODS is lower due to the effect of GB sliding and migration, as shown in Figs. 5(c_2, d_2). In addition, the crack appears primarily at the triple junctions and propagates along the GB.

3.4 Oxidation damage characteristics

Figure 6 shows the SEM images and corresponding EDS maps of failure specimens at 800 °C. The EDS maps present the formation of Al/O-rich oxides along GB, confirming oxidation intrusion at GB and indicating that the variation of ductility may be related to SAGBO. The results suggest that oxygen is highly detrimental in two alloys, especially when oxygen segregates at GB.

In order to assess the oxidative damage, thermal-exposure experiments are performed at temperatures ranging from 600 to 1000 °C with an interval of 100 °C for 1 h. The SEM surface morphologies and corresponding 3D height distributions of the specimens are shown in Fig. 7. For PA-NODS, after being thermally-exposed at 600 °C for 1 h, the sample has a smooth surface with a slight whiteness, and the GB is visible, indicating the slight oxidation. At 700 °C, the surface becomes rougher with a large number of loosely attached white particles, and GB is still visible. As the temperature increases to 800 °C, the surface of the sample is covered with white particles and becomes extremely rough, visible as a

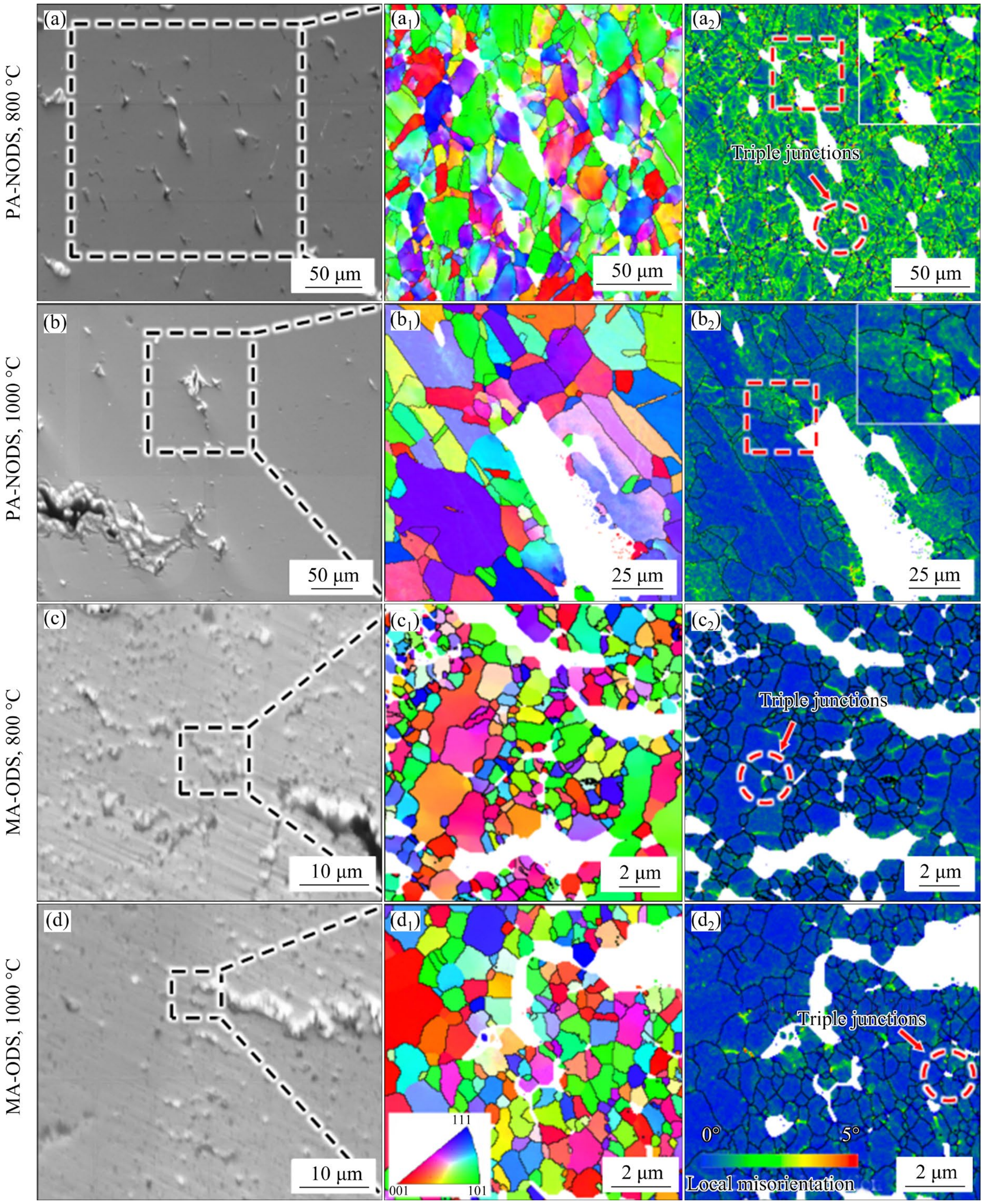

Fig. 5 SEM images (a, b, c, d), IPF images (a_1, b_1, c_1, d_1) and local misorientation images (a_2, b_2, c_2, d_2) perpendicular to fracture surface at 800 and 1000 °C

thick and uneven oxide layer, and GB is no longer detectable, suggesting the formation of thick oxide scales on the surface at 800 °C. However, a few white particles can be seen on the surface, and GB becomes clear again at 900 °C. It is speculated that the poor bonding power between the oxide layer and the matrix causes it to peel off. At 1000 °C, the surface of the sample is covered with rough particles, and the GB becomes indiscernible once more. The surface evolution of the samples can be seen more clearly in the corresponding 3D height distribution. Compared to PA-NODS, the surfaces

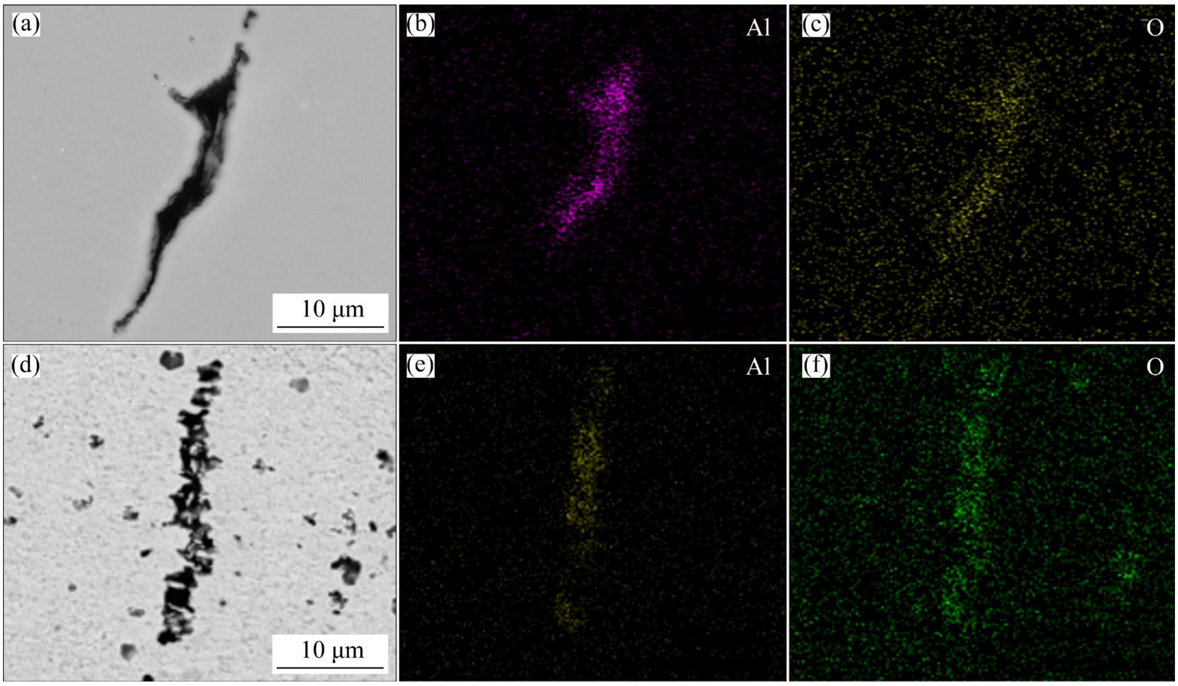

Fig. 6 SEM images (a, d) and corresponding EDS maps (b, c, e, f) of cross-sectional cracks showing formation of Al-rich oxidation products at 800 °C: (a−c) PA-NODS; (d−f) MA-ODS

of MA-ODS are compact and smooth, with no significant changes observed below 800 °C. However, as the temperature increases to 900 °C, the surface becomes rough and covered with white particles. The formation of a thick oxide layer is indicated by the increase and coarsening of the white particles at 1000 °C.

To confirm the oxidation products generated on the oxide layer, the samples of PA-NODS and MA-ODS oxidized at 800 and 1000 °C for 1 h were analyzed by XRD, as shown in Figs. 8(a, b), respectively. The results indicate that the main oxides of the oxide layer are Cr_2O_3, TiO_2, and Al_2O_3.

Figure 9 shows cross-sectional morphologies of samples exposed at 800−1000 °C for 1 h. The spallation protrusions of fracture are observed on the surface of PA-NODS at 800 °C. An oxide layer with a thickness of about 0.4 μm can be detected in PA-NODS, together with the oxidation results of PA-NODS (Fig. 7), indicating that the oxide layer of PA-NODS peels off, which also explains the disappearance of the rough oxide layer on the surface of PA-NODS at 900 and 1000 °C. MA-ODS has better oxidation resistance than PA-NODS due to the more compact oxide layer. In general, the oxide layers of both alloys become significantly thicker with increasing temperature, especially at 1000 °C. Furthermore, the observation of oxidation intrusion in the specimens is verified by the results presented in Fig. 6.

The elemental line distributions along the red lines in Fig. 9 for PA-NODS and MA-ODS after being thermally-exposed at 800 and 900 °C for 1 h are shown in Figs. 10(a, b), respectively. Combined with the XRD analysis results in Fig. 8, the oxides indicated by the arrow in Fig. 9 can be clearly identified. Cr_2O_3, Al_2O_3 and TiO_2 have been verified through the elemental line distribution. Furthermore, an external grey layer of Cr_2O_3-embedded dark TiO_2 and Al_2O_3 is observed in the alloys, which is consistent with the results observed in other superalloys [38].

The thickness of oxide layer thermally-exposed at 1000 °C is obviously larger than that at other temperatures. Since Cr, Al and Ti are prone to react with O_2 to form Cr_2O_3, Al_2O_3 and TiO_2, respectively. This reaction can be represented by the following equation [38]:

$$aX+\frac{b}{2}O_2=X_aO_b \quad (X=Cr,\ Al\ or\ Ti) \tag{2}$$

Moreover, some studies have shown that nanoparticles act as vacancy traps, providing more

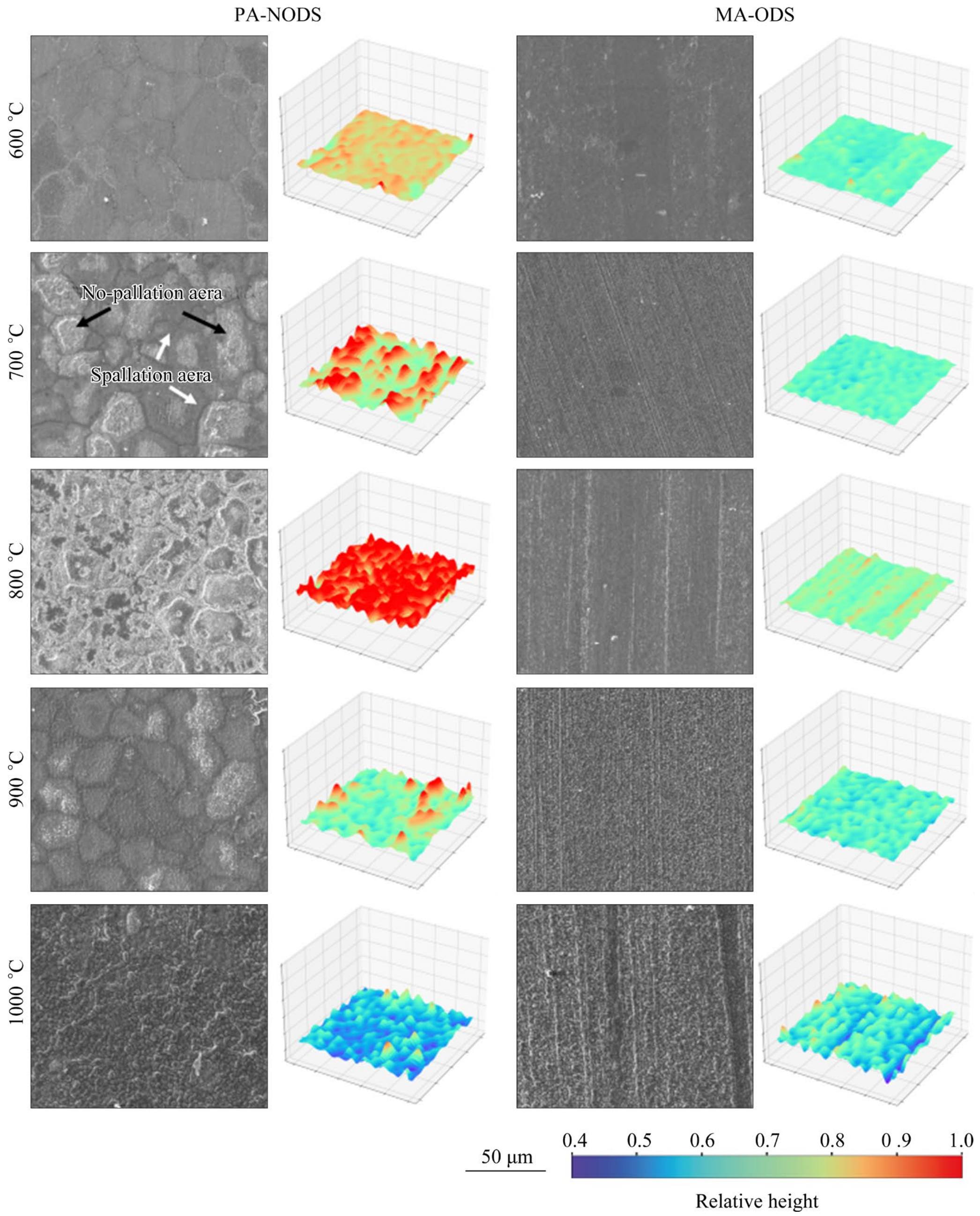

Fig. 7 SEM micrographs and corresponding 3D height distribution images of oxygen attack on samples surface for 1 h at temperatures ranging from 600 to 1000 °C

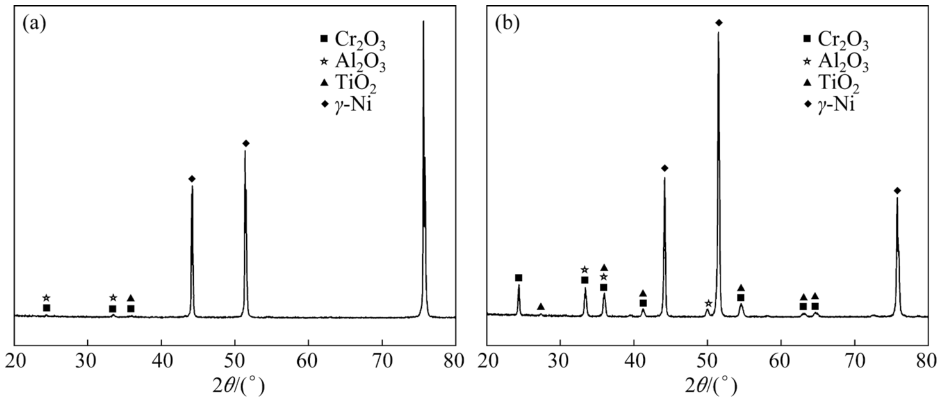

Fig. 8 XRD patterns of alloys after oxidation for 1 h: (a) PA-NODS, at 800 °C; (b) MA-ODS, at 1000 °C

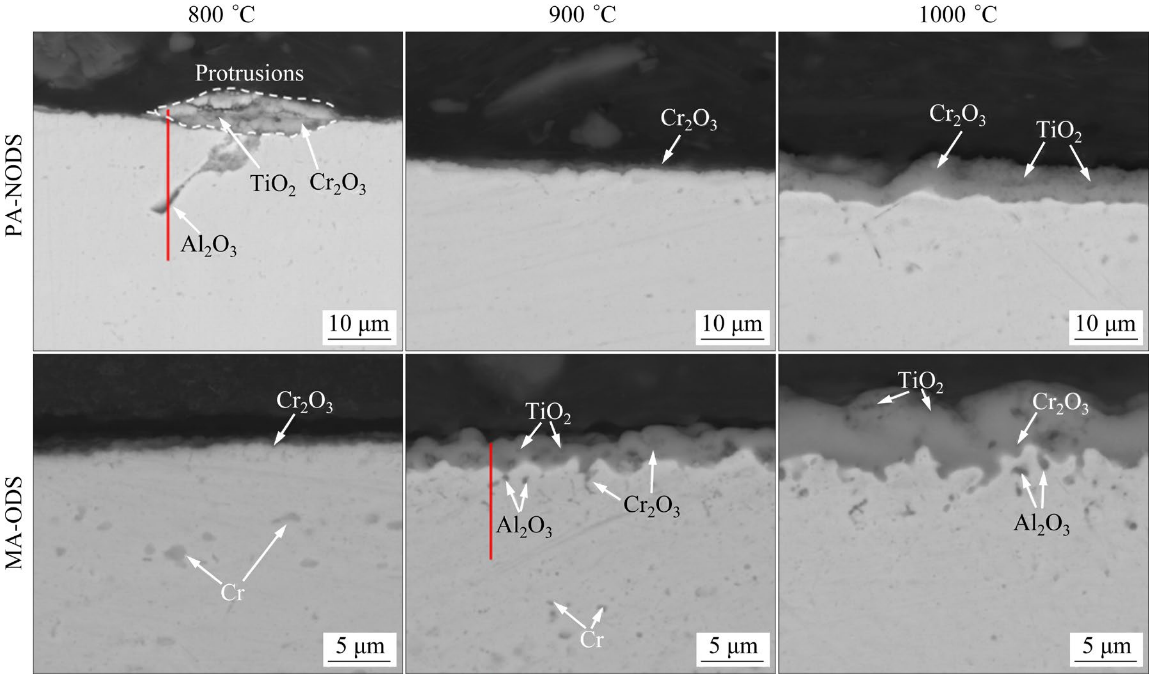

Fig. 9 Cross-sectional images of specimens after being thermally-exposed for 1 h at different temperatures

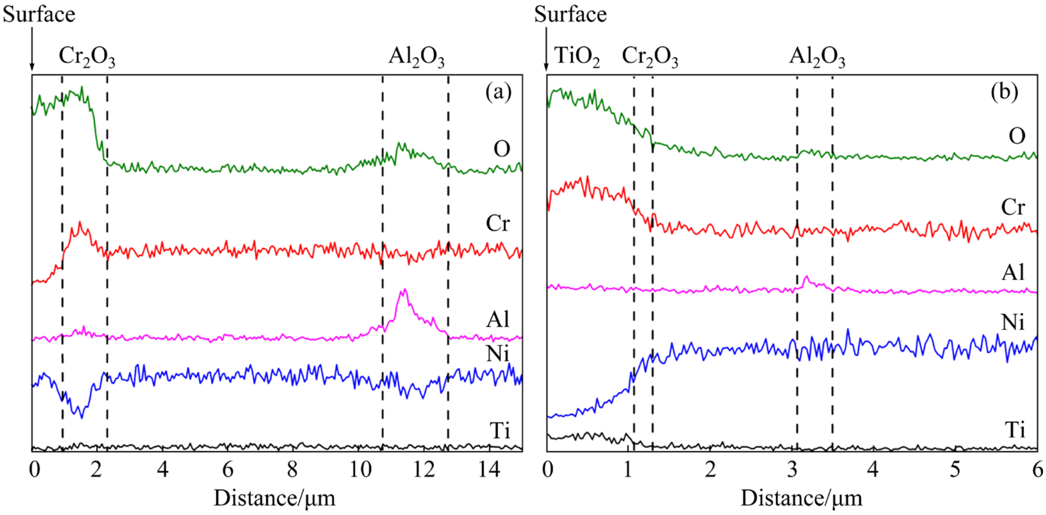

Fig. 10 Elemental line distributions detected by EDS (red lines in Fig. 9) perpendicular to surface of PA-NODS (a) and MA-ODS (b) after exposure for 1 h at 800 and 900 °C, respectively

nucleation points (particle/matrix interface), especially in the near surface region where defects greatly increase the nucleation point position. This can effectively shorten the distance between adjacent Cr_2O_3 nucleation points, reducing the time required for Cr_2O_3 to grow laterally and form a complete oxide layer, i.e., shortening the transient oxidation time [39,40]. This also inhibits the oxidation of other metallic elements in the matrix and reduces the oxidation growth rate. Furthermore, dispersed nanoparticles improve the stability of the matrix, thereby improving the anti-stripping performance of the oxide layer [41]. Therefore, it is reasonable to explain that MA-ODS has better oxidation resistance than PA-NODS.

4 Discussion

4.1 Strengthening mechanism and model

It is well known that the strengthening of nickel-based superalloys can be divided into solid-solution strengthening (σ_{ss}), GB strengthening

(σ_g), dislocation strengthening (σ_d) and nanoparticle strengthening (σ_p).

In this work, the solid-solution strengthening of samples due to Cr, Al, Ti and Fe elements can be expressed as follows [42]:

$$\sigma_{ss}=\left(\sum_i k_i^{1/n} c_i\right)^n \tag{3}$$

where k_i and c_i are the strengthening constant and atomic fraction of solute i, respectively. In this work, n is taken as 0.5, k_{Cr}=337 MPa$^{1/2}$, k_{Al}=225 MPa$^{1/2}$, k_{Ti}=775 MPa$^{1/2}$ and k_{Fe}=153 MPa$^{1/2}$ [43].

Hall−Petch relationship is used to calculated GB strengthening [34,42]:

$$\sigma_g=\frac{k}{\sqrt{d}} \tag{4}$$

where k is the strength constant (5538 MPa·nm$^{1/2}$) [44], and d is average grain diameter.

The dislocation strengthening can be expressed by the Bailey−Hirsch equation [45]:

$$\sigma_d=\alpha MGb\sqrt{\rho_d} \tag{5}$$

where α is a microstructural parameter (1/3) [46], G denotes shear modulus (80 GPa) [47], and M is the Taylor factor (3) [48]. The dislocations density (ρ_d) can be derived from Eq. (1).

In addition, nanoparticle strengthening plays an important role in nickel-based ODS superalloys. It can be illustrated by Eqs. (6)−(8) [45,49]:

$$\sigma_p=M\frac{0.4Gb\ln(2r/b)}{\pi\lambda\sqrt{(1-\nu)}} \tag{6}$$

$$f_v=\frac{N\frac{4}{3}\pi r_p^3}{SD} \tag{7}$$

$$\lambda=r\left[\sqrt{\frac{3\pi}{4f_v}}-1.46\right] \tag{8}$$

where ν is the Poisson ratio (0.291) [48], f_v and λ are the volume fraction and mean spacing of the nanoparticles, respectively, N is the number of the nanoparticles, r is the average radius of the nanoparticles, and S and D (50 nm) are the area and thickness of the sample, respectively, assessed using TEM images.

The YS model of nickel-based ODS superalloys at room temperature is widely accepted [20]:

$$\sigma_y=\sigma_0+\sigma_{ss}+\sigma_g+\sqrt{\sigma_d^2+\sigma_p^2} \tag{9}$$

where σ_0 is the Peierls–Nabarro friction force in pure nickel (8 MPa) [48].

Table 2 lists the comparison of calculated and experimental values for these two alloys. As calculated above, the YS of the samples originates from the GB strengthening and dispersion strengthening. The predicted value is very close to the experimental value, as shown in Fig. 11.

Table 2 Calculated σ_0, σ_{ss}, σ_g, σ_d, σ_p and σ_y values compared with experimental σ_y values of samples at room temperature (MPa)

Alloy	σ_0	σ_{ss}	σ_g	σ_d	σ_p	Calculated σ_y	Experimental σ_y
PA-NODS	8	175.0	55.0	209.7	–	445.7	324.5
MA-ODS	8	175.0	234.0	464.7	489.5	1092.0	1020

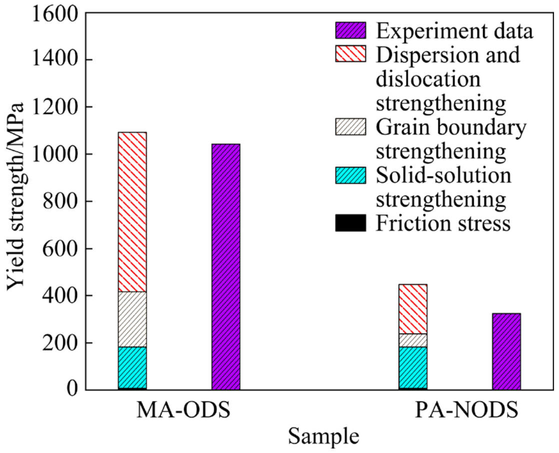

Fig. 11 Comparison between experimental and estimated yield strength for alloys

4.2 Mechanism of ductility variation

The SEM and EDS images of the fracture cross-sections in the specimens present that the ductility is affected by the oxidative damage. Therefore, the decrease in ductility of PA-NODS below 800 °C can be reasonably explained by the dislocation accumulation at GB and oxidation damage, which is consistent with the damage mechanism of intergranular oxidation attack and the reports on other polycrystalline superalloys [17,50−53]. Meanwhile, there is a slight variation in the ductility of MA-ODS below 600 °C, which contributes to its excellent oxidation resistance. However, as the temperature increases to 800 °C,

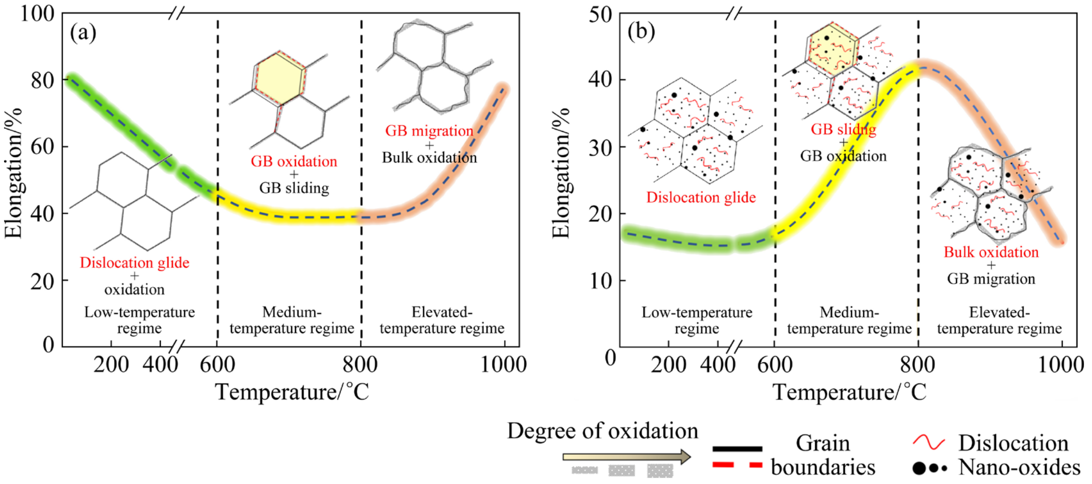

Fig. 12 Schematic diagrams of mechanism of ductility variation in nickel-based superalloys without ODS phase (a) and nickel-based ODS superalloys (b) at different temperatures

the thermal activation increases, and the UFG with high-density GBs are easy to slide, thus relieving stress concentration and increasing the ductility of MA-ODS [14].

At elevated-temperature regime, the ductility of PA-NODS increases, although the oxidative damage accelerates, which can be explained as follows. The improved temperature due to more adiabatic heating enhances GB sliding and migration, and reduces dislocation accumulation. The local misorientation images (Fig. 5) confirm that the local stress is significantly relieved, and the ductility of PA-NODS recovers. In addition, although grain boundary sliding and migration are beneficial to improving ductility, the accelerated oxidation rate and oxidation intrusion of GB observed in Figs. 5−8 indicate that oxidation damage is the dominant factor in decreasing the ductility of MA-ODS.

In conclusion, oxidation, GB sliding and migration play a dominate role in the ductility evolution of nickel-based superalloys with increasing temperature, which is primarily associated with grain size and nanoparticles of the alloys. The nanoparticles act as vacancy traps, providing more nucleation points (particle/matrix interface), especially in the near surface region where defects greatly increase the nucleation point. This can effectively shorten the distance between adjacent Cr_2O_3 nucleation points, reducing the time required for Cr_2O_3 to grow laterally and form a complete oxide layer, i.e., shortening the transient oxidation time. This also inhibits the oxidation of other metallic elements in the matrix and reduces the oxidation growth rate. Furthermore, dispersed nanoparticles improve the stability of the matrix, thereby improving the anti-stripping performance of the oxide layer. The mechanism of ductility variation in nickel-based superalloys with different grain sizes and nanoparticles plotted against temperature can be illustrated in Fig. 12.

5 Conclusions

(1) The microstructure analysis and strength model show that the contribution of grain boundary strengthening, dislocation strengthening and nanoparticle strengthening of MA-ODS exceeds 83%, resulting in significantly higher strength of MA-ODS than PA-NODS at low temperature.

(2) Cr_2O_3, Al_2O_3 and TiO_2 are formed on the surface of the alloys after thermal exposure for 1 h in the temperature range of 600−1000 °C, and MA-ODS exhibits excellent oxidation resistance.

(3) The alloy has transgranular fracture below 600 °C. With the increase of temperature, the crack source appears primarily at triple junctions and propagates along grain boundaries, and intergranular fracture becomes the main fracture mode. Moreover, oxidation intrusion at the grain boundary accelerates the fracture of the alloy.

(4) The oxidative damage at grain boundaries decreases the ductility of PA-NODS below 800 °C, but the grain boundary sliding and migration increase the ductility above 800 °C. For MA-ODS, there is no significant variation in ductility below

600 °C. As the temperature increases to 800 °C, the ductility increases to a maximum of 47.3% due to its excellent oxidation resistance and grain boundary sliding. Above 800 °C, although grain boundary sliding and migration are beneficial to improving ductility, accelerated oxidation damage can lead to a decrease in ductility.

CRediT authorship contribution statement

Wu-qiang HE: Writing − Original draft, Methodology, Funding acquisition, Formal analysis; **Ping KE** and **Jing-yue HUANG:** Visualization, Investigation; **Feng LIU:** Software, Resources; **Lan HUANG:** Conceptualization, Software, Resource; **Li-ming TAN:** Writing − Review & editing; **Shi-wen HE:** Project administration, Formal analysis; **Cui LAI:** Writing − Review & editing, English correction; **Cai-he FAN:** Data curation.

Declaration of competing interest

The authors declare that they have no known competing financial interests or personal relationships that could have appeared to influence the work reported in this paper.

Data availability statement

The raw data related to this manuscript will be made available upon request.

Acknowledgments

This work was supported by the National Natural Science Foundation of China (No. 52271177), Leading Talents Project of Scientific and Technological Innovation in Hunan Province, China (No. 2021RC4036), the Natural Science Foundation of Hunan Province, China (Nos. 2023JJ50172, 2020JJ6069), and State Key Laboratory of Materials Processing and Die & Mould Technology, Huazhong University of Science and Technology, China.

References

[1] LI Fang, YUAN Ding-ling, CHEN Kang-hua, CHEN Song-yi, LI Li. A novel creep model with synergetic Orowan bypassing and climbing mechanisms in nickel-base superalloys [J]. Transactions of Nonferrous Metals Society of China, 2024, 34 (4): 1167−1177.

[2] SHIN W S, BAIK S I, SEIDMAN D N, LEE K A, PARK C, KIM Y J. Analysis of antioxidation behavior of cryo-milled oxide-dispersion-strengthened ferritic steel incorporated with formation of Y−Ti−O(N) nano-precipitates [J]. Acta Materialia, 2022, 225: 117589.

[3] UKAI S, TAYA K, NAKAMURA K, AGHAMIRI M S, OONO N, HAYASHI S, OKUDA T. Directional recrystallization by zone annealing in a Ni-based ODS superalloy [J]. Journal of Alloys and Compounds, 2018, 744: 204−210.

[4] ZHAO Tian-yang, FU Pei, CHEN Zhou, ZHOU Ping, LI Chao. Calculation of phase transformation latent heat based on cooling curves in end-quench test and its application in nickel-based superalloy [J]. Transactions of Nonferrous Metals Society of China, 2022, 32(5): 1718−1727.

[5] HONG K H, KIM J H, CHANG K, KWON J. The role of Cr on oxide formation in Ni−Cr alloys: A theoretical study [J]. Computational Materials Science, 2018, 142: 185−191.

[6] ESKANDARANY EL, SHERRIF M. The history and necessity of mechanical alloying [M]. 3nd ed. William Andrew Publishing, 2020.

[7] XU Hai-jian, LI Wei-juan, SHA Xiao-chun, MENG Jing-song, KANG Chao, WANG Wen-zhong, ZANG Xi-min, WANG Zhao-dong. Effects of Zr addition on the microstructural stability of 15Cr-ODS steels under elevated-temperature annealing [J]. Fusion Engineering and Design, 2019, 138: 231−238.

[8] HE Wu-qiang, LIU Feng, TAN Li-ming, HUANG Lan, HE Shi-wen, ZHANG Li-ke, FAN Cai-he. Investigation on different additions as candidates for nano-oxide particles in nickel-based ODS superalloys [J]. Materials Characterization, 2024, 209: 113648.

[9] PONRAJ B V, KUMARAN S. Facile in-situ dispersion of $Y_2Ti_2O_7$ during mechanical alloying of oxide dispersion strengthened ferritic steels [J]. Materials Letters, 2020, 278: 128439.

[10] PARK J, JANG J, KIM T K, KIM S J, AHN J H. Formation of nanostructures in Ni−22Cr−11Fe−1X (X=Y_2O_3, TiO_2) alloys by high-energy ball-milling [J]. Journal of Nanoscience and Nanotechnology, 2011, 11(7): 6213−6218.

[11] DURGA P V, PRASAD K S, CHANDRASEKHAR S B, REDDY A V, BAKSHI S R, VIJAY R. Microstructural and mechanical properties of oxide dispersion strengthened iron aluminides produced by mechanical milling and hot extrusion [J]. Journal of Alloys and Compounds, 2020, 834: 155218.

[12] WANG Kai-meng, JING Hong-yang, XU Lian-yong, ZHAO Lei, HAN Yong-dian, LI Hai-zhou, SONG Kai. Microstructure evolution of 55Ni−23Cr−13Co nickel-based superalloy during high-temperature cyclic deformation [J]. Transactions of Nonferrous Metals Society of China, 2021, 31(11): 3452−3468.

[13] JIANG R, REED P A S. Critical Assessment 21: oxygen-assisted fatigue crack propagation in turbine disc superalloys [J]. Materials Science and Technology, 2016, 32(5): 401−406.

[14] YU Li, LU Zheng, XIAN Jia-bei, CHEN Xuan-yu, PENG Shi-bo, LI Xiao-long, LI Hui. Effects of Al content on microstructure and tensile properties of Ni-based ODS superalloys [J]. Journal of Alloys and Compounds, 2023, 941: 168965.

[15] LI H Y, SUN J F, HARDY M C, EVANS H E, WILLIAMS S J, DOEL T J A, BOWEN P. Effects of microstructure on high temperature dwell fatigue crack growth in a coarse grain PM

nickel based superalloy [J]. Acta Materialia, 2015, 90: 355−369.

[16] KITAGUCHI H S, LI H Y, EVANS H E, DING R G, JONES I P, BAXTER G, BOWEN P. Oxidation ahead of a crack tip in an advanced Ni-based superalloy [J]. Acta Materialia, 2013, 61: 1968−1981.

[17] NÉMATH A A N, CRUDDEN D J, ARMSTRONG D E J, COLLINS D M, LI K, WILKINSON A J, GROVENOR C R M, REED R C. Environmentally-assisted grain boundary attack as a mechanism of embrittlement in a nickel-based superalloy [J]. Acta Materialia, 2017, 126: 361−371.

[18] YE Wen-ming, HU Xu-teng, SONG Ying-song. The relationship between creep and tensile properties of a nickel-based superalloy [J]. Materials Science and Engineering A, 2020, 774: 138847.

[19] XU Jing-hao, GRUBER Hans, DENG Dun-yong, PENG R L, MOVERARE J J. Short-term creep behavior of an additive manufactured non-weldable nickel-base superalloy evaluated by slow strain rate testing [J]. Acta Materialia, 2019, 179: 142−157.

[20] KONG T, KANG B, RYU H J, HONG S H. Microstructures and enhanced mechanical properties of an oxide dispersion-strengthened Ni-rich high entropy superalloy fabricated by a powder metallurgical process [J]. Journal of Alloys and Compounds, 2020, 839: 155724.

[21] ZHANG He, LI Zhi-bo, DENG Xiao-chun, CHEN Ben, ZHANG Guo-hua, CHOU K C. Effects of various rare earth oxides on morphology and size of oxide dispersion strengthening (ODS)-W and ODS-Mo alloy powders [J]. Transactions of Nonferrous Metals Society of China, 2022, 32(8): 2665−2680.

[22] HE Wei-lin, MENG Bao, SONG Bing-yi, WAN Min. Grain size effect on cyclic deformation behavior and springback prediction of Ni-based superalloy foil [J]. Transactions of Nonferrous Metals Society of China, 2022, 32(4): 1188−1204.

[23] TOREMEIER T C, LILLO T M, SIMPSON J A. Elevated temperature strength of fine-grained INCONEL alloy MA754 [J]. Metallurgical and Materials Transactions A, 2005, 36(9): 2552−2555.

[24] KLUEH R L, SHINGLEDECKER J P, SWINDEMAN R W, HOELZER D T. Oxide dispersion-strengthened steels: A comparison of some commercial and experimental alloys [J]. Journal of Nuclear Materials, 2005, 341: 103−114.

[25] XIA Tian, XIE Yue-huang, YANG Chao, ZENG Wei, BI Zhong-nan, LIANG Jia-miao, ZHU Guo-liang, WANG Jun, ZHANG De-liang, LAVERNIA E J. Strengthening effects and thermal stability of the ultrafine grained microstructure of a nickel base superalloy at room and elevated temperatures [J]. Materials Characterization, 2018, 145: 362−370.

[26] AUGER M A, DE CASTRO V, LEGUEY T, LOZANO-PEREZ S, BAGOT P A J, MOODY M P, ROBERTS S G. Effect of the milling atmosphere on the microstructure and mechanical properties of a ODS Fe−14Cr model alloy [J]. Materials Science and Engineering A, 2016, 671: 264−274.

[27] AUGER M A, LEGUEY T, MUÑOZ A, MONGE M A, DE CASTRO V, FERNÁDEZ P, GARCÉS G, PAREJA R. Microstructure and mechanical properties of ultrafine-grained Fe−14Cr and ODS Fe−14Cr model alloys [J]. Journal of Nuclear Materials, 2011, 417: 213−216.

[28] CASTRO D V, LEGUEY T, MUÑOZ A, MONGE M A, FERNÁDEZ P, LANCHA A M, PAREJA R. Mechanical and microstructural behaviour of Y_2O_3 ODS EUROFER 97 [J]. Journal of Nuclear Materials, 2007, 367/368/369/370: 196−201.

[29] MCCLINTOCK D A, SOKOLOV M A, HOELZER D T, NANSTAD R K. Mechanical properties of irradiated ODS-EUROFER and nanocluster strengthened 14YWT [J]. Journal of Nuclear Materials, 2009, 392: 353−359.

[30] LI Shao-fu, ZHOU Zhang-jian, LI Ming, WANG Man, ZHANG Guang-ming. Microstructure characterization and tensile properties of 18Cr−4Al-oxide dispersion strengthened ferritic steel [J]. Journal of Alloys and Compounds, 2015, 648: 39−45.

[31] LIU Tong, WANG Lin-bo, WANG Chen-xin, SHEN Hai-long, ZHANG Hong-tao. Feasibility of using $Y_2Ti_2O_7$ nanoparticles to fabricate high strength oxide dispersion strengthened Fe−Cr−Al steels [J]. Materials & Design, 2015, 88: 862−870.

[32] GAO R, XIA L L, ZHANG T, WANG X P, FANG Q F, LIU C S. Oxidation resistance in LBE and air and tensile properties of ODS ferritic steels containing Al/Zr elements [J]. Journal of Nuclear Materials, 2014, 455: 407−411.

[33] MICHLER T, BALOGH M P. Hydrogen environment embrittlement of an ODS RAF steel – Role of irreversible hydrogen trap sites [J]. International Journal of Hydrogen Energy, 2010, 35(18): 9746−9754.

[34] WANG Zhang-wei, LU Wen-jun, ZHAO Huan, LIEBSCHER C H, HE Jun-yang, PONGE D, RAABE D, LI Zhi-ming. Ultrastrong lightweight compositionally complex steels via dual-nanoprecipitation [J]. Science Advances, 2020, 6(46): eaba9543.

[35] TAN Li-ming, HUANG Zai-wang, LIU Feng, HE Guo-ai, WANG Xin, HUANG Lan, ZHANG Yi-wen, JIANG Liang. Effects of strain amount and strain rate on grain structure of a novel high Co nickel-based polycrystalline superalloy [J]. Materials & Design, 2017, 131: 60−68.

[36] GONG He, CHEN Chang-hong, YAO Yao. A void evolution-based damage model for ductile fracture of metallic materials [J]. Journal of Micromechanics and Molecular Physics, 2019, 4(4): 1950008.

[37] BURBERY N B, PO G, DAS R, GHONIEM N, FERGUSON W G. Dislocation dynamics in polycrystals with atomistic-informed mechanisms of dislocation-grain boundary interactions [J]. Journal of Micromechanics and Molecular Physics, 2017, 2(1): 1750003.

[38] YE Xian-jue, LI Yun-ping, AI Yan-ling, NIE Yan. Novel powder packing theory with bimodal particle size distribution-application in superalloy [J]. Advanced Powder Technology, 2018, 29(9): 2280−2287.

[39] GABRIELE D F, AMORE S, SCAIOLA C, ARATO E, GIURANNO D, NOVAKOVIC R, RICCI E. Corrosion behaviour of 12Cr-ODS steel in molten lead [J]. Nuclear Engineering and Design, 2014, 280: 69−75.

[40] DRYEPONDT S, TURAN J, LEONARD D, PINT B A. Long-term oxidation testing and lifetime modeling of cast

and ODS FeCrAl alloys [J]. Oxidation of Metals, 2017, 87: 215−248.

[41] JÖNSSON B, LU Q, CHANDRASEKARN D, BERGLUND R, RAVE F. Oxidation and creep limited lifetime of Kanthal APMT®, a dispersion strengthened FeCrAlMo alloy designed for strength and oxidation resistance at high temperatures [J]. Oxidation of Metals, 2013, 79: 29−39.

[42] YU Li, LU Zheng, LI Xiao-long, PENG Shi-bo, LI Hui. Effect of Zr and Hf addition on microstructure and tensile properties of high-Al Ni-based ODS superalloys [J]. Materials Science and Engineering A, 2022, 854: 143811.

[43] AHMADI M R, POVODEN-KARADENIZ E, WHITMORE L, STOCKINGER M, FALAHATI A, KOZESCHNIK E. Yield strength prediction in Ni-base alloy 718Plus based on thermo-kinetic precipitation simulation [J]. Materials Science and Engineering A, 2014, 608: 114−122.

[44] BUI Q H, DIRRAS G, RAMTANI S, GUBICZA J. On the strengthening behavior of ultrafine-grained nickel processed from nanopowders [J]. Materials Science and Engineering A, 2010, 527: 3227−3235.

[45] WANG Guo-wei, HUANG Lan, ZHAN Xin, TAN Li-ming, QIN Zi-jun, HE Wu-qiang, LIU Feng. Strength-hardness correlations of thermal-exposed oxide dispersion strengthened nickel-based superalloy with different grain size distributions [J]. Materials Characterization, 2021, 178: 111178.

[46] PRAUD M, MOMPIOU F, MALAPLATE J, CAILLARD D, GARNIER J, STECKMETER A, FOURNIER B. Study of the deformation mechanisms in a Fe−14%Cr ODS alloy [J]. Journal of Nuclear Materials, 2012, 428: 90−97.

[47] SERAFINI A, ANGELLA G, MALARA C, BRUNELLA M F. Mechanical and microstructural characterization of AF955 (UNS N09955) nickel-based superalloy after different heat treatments [J]. Metallurgical and Materials Transactions A, 2018, 49(11): 5339−5352.

[48] PASEBANI S, DUTT A K, BURNS J, CHARIT I, MISHRA R S. Oxide dispersion strengthened nickel based alloys via spark plasma sintering [J]. Materials Science and Engineering A, 2015, 630: 155−169.

[49] SONG P, YABUUCHI K, SPÄTIG P. Insights into hardening, plastically deformed zone and geometrically necessary dislocations of two ion-irradiated FeCrAl(Zr)-ODS ferritic steels: A combined experimental and simulation study [J]. Acta Materialia, 2022, 234: 117991.

[50] CALMUNGER M, CHAI G, JOHANSSON S, MOVERARE J. Deformation behaviour in advanced heat resistant materials during slow strain rate testing at elevated temperature [J]. Theoretical and Applied Mechanics Letters, 2014, 4(4): 041004.

[51] GABB T P, TELESMAN J, BANIK A, MCDEVITT E. Use of slow strain rate tensile testing to assess the ability of several superalloys to resist environmentally assisted intergranular cracking [C]//8th Int Symp. Hoboken, NJ, USA, John Wiley & Sons Inc, 2014: 697−712.

[52] REZENDE M C, ARAÚJO L S, GABRIEL S B, DILLE J, DE ALMEIDA L H. Oxidation assisted intergranular cracking under loading at dynamic strain aging temperatures in Inconel 718 superalloy [J]. Journal of Alloys and Compounds, 2015, 643(Suppl): s256−s259.

[53] LI Z M, LI X N, HU Y L, ZHENG Y H, YANG M, LI N J, BI L X, LIU R W, WANG Q, DONG C, JIANG Y X, ZHANG X W. Cuboidal γ' phase coherent precipitation-strengthened Cu−Ni−Al alloys with high softening temperature [J]. Acta Materialia, 2021, 203: 116458.

镍基高温合金的力学性能及显微组织演化

何武强 [1,2,3]，柯 平 [1]，黄京悦 [1]，刘 锋 [2,3]，谭黎明 [2,3]，黄 岚 [2,3]，何世文 [1]，赖 萃 [4]，范才河 [1]

1. 湖南工业大学 材料与先进制造学院，株洲 412007；
2. 中南大学 粉末冶金国家重点实验室，长沙 410083；
3. 中南大学 粉末冶金研究院，长沙 410083；
4. 湖南大学 环境科学与工程学院，长沙 410083

摘 要：研究了含和不含氧化物弥散强化(ODDS)相的两种镍基高温合金在不同温度条件下的力学性能和抗氧化性能。采用扫描电镜、电子背散射衍射和透射电镜对其微观结构进行表征。结果表明，含和不含氧化物弥散相的两种镍基高温合金室温屈服强度分别为 1020 MPa 和 324 MPa。构建了两种合金室温屈服强度模型，计算得出镍基 ODS 高温合金的晶界强化、位错强化和纳米颗粒强化的贡献超过 83%。随着温度的升高，晶界滑动和迁移降低了合金的强度，但提高了合金的塑性；而氧化作用降低了合金的塑性，加剧了样品的断裂。镍基 ODS 高温合金在 800 ℃时伸长率达到最大值 47.3%。

关键词：镍基高温合金；氧化物弥散强化相；力学性能；抗氧化性

(Edited by Bing YANG)